Cavitation erosion performance of CrAlYN/CrN nanoscale multilayer coatings deposited on Ti6Al4V by HIPIMS

MA, Dina, HARVEY, Terry, WELLMAN, Richard, EHIASARIAN, Arutiun, HOVSEPIAN, Papken <http://orcid.org/0000-0002-1047-0407>, ARUNPRABHU, Sugumaran, PURANDARE, Yashodhan <http://orcid.org/0000-0002-7544-9027> and WOOD, Robert

Published version

MA, Dina, HARVEY, Terry, WELLMAN, Richard, EHIASARIAN, Arutiun, HOVSEPIAN, Papken, ARUNPRABHU, Sugumaran, PURANDARE, Yashodhan and WOOD, Robert (2019). Cavitation erosion performance of CrAlYN/CrN nanoscale multilayer coatings deposited on Ti6Al4V by HIPIMS. Journal of Alloys and Compounds, 788, 719-728.

Copyright and re-use policy

Cavitation erosion performance of CrAlYN/CrN nanoscale multilayer coatings deposited on Ti6Al4V by HIPIMS

D. Ma [a], T. J. Harvey [a], R. G. Wellman [b], A. P. Ehiasarian [c], P. Eh. Hovsepian *[c],

A. A. Sugumaran [c], Y. P. Purandare [c], R. J. K. Wood [a]

[a] National Centre for Advanced Tribology, nCATS, University of Southampton, Southampton, SO17 1BJ, UK

[b] Surface Engineering, Rolls-Royce plc, Derby, DE24 8BJ, UK

[c] National HIPIMS Technology Centre, Materials and Engineering Research Institute, Sheffield Hallam University, Sheffield, S1 1WB, UK

* Corresponding author: Email: P.Hovsepian@shu.ac.uk. Telephone: +44-114-225 3644

Fax: +44-114-225 3501.

Abstract

Water droplet erosion (WDE) protection of Ti6Al4V turbofan blades is of paramount importance to the aviation industry. A novel CrAlYN/CrN nanoscale multilayer coating deposited by the HIPIMS technique was evaluated as a potential candidate for this application. Literature suggests a strong correlation in performance ranking under WDE and cavitation erosion (CE) tests. Hence, the WDE performance of the CrAlYN/CrN coating on Ti6Al4V was investigated with an ultrasonic cavitation device.

The results show excellent adhesion and superior erosion resistance of the CrAlYN/CrN coating (erosion rate lower by a factor of 14 compared to the bare Ti6Al4V substrate) and compared to coatings reported in the literature with spallation as their main erosion mechanism. Cross-sectional FIB studies revealed formation of substrate cracks underneath

the coating when CE generated stresses exceeded the fatigue strength of the Ti6Al4V alloy. The interfaces of the nanoscale multilayers protected the substrate by forming an effective barrier against shock waves, delayed fatigue crack formation, deflected and arrested any cracks formed impeding the overall coating damage. The research shows that the CE resistance is influenced by the coating's texture and elastic properties, (Young's modulus).

The paper discusses the erosion mechanisms of the coating and the excellent CE protection it offers.

Key words: HIPIMS, Cavitation, Water droplet erosion, Nanoscale multilayers.

1. Introduction:

Water droplet erosion (WDE) causes progressive material loss from a solid surface by continuous impingements of water droplets [1]. It has become a great concern for power generation industry as the leading edge of steam and wind turbine blades suffer from WDE during operation. In the case of aviation industry, WDE takes place when an aircraft flies through rain storm or clouds, the leading edge of turbofan blades suffer from high-speed, (300-400 m/s) impingements of water droplets, resulting in material removal that subsequently changes the leading edge profile. This affects the aerodynamic performance of turbofan blades, which eventually leads to efficiency drop of the aircraft engine.

The rate of erosion due to water droplet impact is not constant with time but exhibits several erosion rate-time patterns. According to ASTM G73-10 standard [2], the evolution of WDE process can be mainly divided in three stages: incubation period, in which there is no measurable erosion damage; maximum erosion rate stage, where the erosion rate increases to its maximum and remains constant; and the deceleration stage, in which the erosion rate starts to decline. This study has an emphasis on the incubation period of WDE, in which the primary damage mechanism is induced by water-hammer pressure (the magnitude of which ranges in hundreds of MPa). Upon impingement the high impact pressure and stress waves exerted into the exposed surface results in structural damage that contributes to the drastic increase of erosion rate in the later stages [1, 3-5]. Previous research indicates a correlation in damage mechanism of WDE and cavitation erosion (CE) [6, 7]. During the CE process, microjets are formed by asymmetric implosion of cavitation bubbles on solid surface, generating high impact pressure and stress waves [8]. It is reported that material performance ranking display similarity under the WDE and CE tests, hence, CE has frequently been considered by investigators to predict WDE behaviour. Additionally, it is proposed as a

screening process for WDE in ASTM G73 [2]. Therefore, in this study CE test has been introduced.

Many attempts have been made to correlate the WDE resistance to single mechanical property; however no universal agreement has been established. Researchers [5, 9–13] propose that WDE is a complicated process and that a combination of material properties should be considered when combatting such a phenomenon. Additionally, water droplet impingement is a dynamic loading process with a high strain rate, hence, dynamic mechanical properties are applicable [14]. In the case of coating applications, in addition to the premise of a strong adhesion to the substrate, a hard yet tough surface is desired. The ideal coating surface should not only resist the high impact pressure, but also inhibit stress wave reinforcements at the interface [15]. Employment of various hard coatings for WDE resistance has been tried in the past studies, however, their failure caused by brittle fracture and delamination due to poor adhesion have been reported. Improvement of toughness while maintaining the hardness is the challenge for such application. Deposition of nanoscale multilayer microstructure is one of the most advantageous approaches to improve toughness of thin films and is achieved via the following three main mechanisms: crack deflection at interfaces between layers, ductile interlayer ligament bridging and crack tip blunting due to nanoplasticity at the interface [16]. Furthermore, it was shown that in superlattice structured coatings a significant fracture toughness enhancement can be achieved (for e.g. by factor of two for the TiN/CrN system) in a way similar to the superhardening effect reported for these structures [17]. With the introduction of the novel High Power Impulse Magnetron Sputtering (HIPIMS) technique, very dense and defect free nanoscale multilayer coatings with high adhesion can be deposited. The unique properties of the layered structures deposited by HIPIMS technique, such as crack deflection at the sharp and flat interfaces and their role as sites for elastic energy dissipation, also add to the established mechanisms responsible for the

enhancement of the mechanical properties. HIPIMS utilises transient impulse (short pulses) glow discharge with a very high power and current density which translates to high plasma densities and ionised metal particles [18]. The utilisation of highly ionised metal fluxes during the surface pre-treatment and coating deposition stages allow fine-tuning of the metallurgical reactions at the coating-substrate interface as well as precise control over the coating structure, crystallographic orientation, and surface morphology.

This study will investigate the potential usage of HIPIMS deposited nanoscale multilayer CrAlYN/CrN coatings to protect Ti6Al4V substrate against WDE. The results will be compared with monolayer TiN which is one of the most established and popular coatings due to its high hardness and wear resistance, [19].

2. Materials and methods:

2.1 Coating deposition.

Nanoscale multilayer CrAlYN/CrN coatings were deposited in an industrial size HTC 1000-4, coating system, (Hauzer Techno Coatings, Europe B.V., Venlo, The Netherlands) equipped with four unbalanced magnetron sources, which can be operated in HIPIMS mode. The HIPIMS plasma was generated using dedicated High-pulse 4008 power supplies (Hüttinger Elektronik Sp. z o.o., Warsaw, Poland). Prior to coating deposition, adhesion enhancing pre-treatment of substrates was carried out with the help of HIPIMS plasma sustained on a Cr target [20]. Coating deposition was carried out using CrAlY, CrAl and Cr targets in a mixed reactive Ar+N_2 (ratio 1:1) atmosphere at 400 °C. The coating architecture comprises of CrAlYN base layer followed by alternating nanoscale CrAlYN and CrN multilayers. In this study 2 sets of multilayer coatings were deposited by manipulating the ion energies available from the depositing flux; one with high and one with low ion bombarding energies and

henceforth will be referred to as coating C1 and coating C2 respectively. The substrates were subjected to three-fold rotation to assist uniform distribution of depositing flux over the surface of substrates. Various types of polished samples from Ti6Al4V, 304 L stainless steel (SS) and HRc = 62 hardened high speed steel (HSS) were coated for thorough characterisation of the coatings.

2.2 Coating characterisation.

Various analytical techniques were employed to characterise the coatings.

Coating adhesion was measured by the Daimler Benz (DB) Rockwell indentation test, (ISO 26443) as well as a progressive loading scratch test (maximum load: 80 N) conducted on CSEM-Anton Paar REVETEST, (ISO 20502). Coated HSS and Ti6Al4V alloy substrates were used for these tests.

The Knoop hardness of the coatings (HSS substrate) was investigated with the help of Mitotoyo microhardness tester using a 0.25 N load (hold time of 10 seconds).

The texture of the nanoscale multilayer structure (304L SS substrates) was investigated using Brag-Brentano (BB) geometry (20°-130° with a scan rate of 0.008 degrees per second) X-Ray Diffraction (XRD) technique (PHILIPS XPERT). Texture coefficient (T*) was calculated using the following equation [21, 22]:

$$T^* = \frac{I_{hkl}/R_{hkl}}{(1/n)\sum_0^n (I_{hkl}/R_{hkl})} \qquad (1),$$

where $I_{(hkl)}$ is the measured peak intensity from the (hkl) reflections, R_{hkl} is the reference standard (random) peak intensity from the (hkl) reflections and n is the number of reflections considered. The JCPDS values of peak intensity were used as the standard reference (R_{hkl})

intensity values since it was not possible to determine R_{hkl} intensity values for a randomly oriented coating material.

Detailed analysis of the coating microstructure in terms of its nanoscale multilayer architecture, interfaces, epitaxy and density among the columnar grains was carried out using bright field Transmission Electron Microscopy (Philips STEM 420 equipped with a LaB6 filament). Coatings deposited on SS substrates were used for TEM work whereas a FEI QUANTA 3D FEG - SEM was used for the focused ion beam (FIB) milling and imaging cross-sections of the coatings deposited on Ti6Al4V alloy at the point of interest after the CE tests.

Glancing angle geometry XRD technique was used for determining the residual stress in the coatings (SS substrates). The angle of incidence to the substrate was fixed at a low angle of 2º where a scan rate of 0.008 degrees per second was employed. Residual Stress (σ) was calculated from the slope of the least-squares fit of the plot of a_Ψ versus $\sin^2\Psi$ and using the following expression

$$\sigma = \frac{\text{Slope E}}{a_\Psi\,(1+\nu)} \qquad (2),$$

where E is the elastic modulus, a_Ψ is the lattice parameter and ν (0.3) is the Poisson's ratio [22]. The elastic modulus E was determined by nanoindentation test. A nano hardness tester (CSEM-Anton Paar) with a Berkovich indenter was used to evaluate the elastic modulus of the coatings. The applied load for all of the elastic modulus measurements was 30 mN. The lattice parameter a_Ψ can be calculated for each diffraction peak where Ψ is the angle between the diffraction vector of planes (hkl) and the normal to the surface, such that $\Psi = \theta - \gamma$ where θ is the Bragg angle and γ is the angle of incidence of the X-ray beam relative to the specimen surface.

2.3 Cavitation erosion test.

An ultrasonic induced cavitation device (UIP 1000 hdt) was used to carry out the CE tests. The tests were performed in distilled water bath maintained at laboratory temperature (~ 25 ± 2 °C); procedures followed the ASTM G32-92 standard. The CrAlYN / CrN coated and uncoated Ti6Al4V specimens were set opposite to a vibrating tip of titanium sonotrode. Cavitation was induced by longitudinal oscillation at 20 kHz at peak-to-peak amplitude of 50 μm. The titanium tip (grade 5) of the vibrating horn was 18 mm in diameter. A stand-off distance between the tip of the sonotrode and surface of the specimen was set to 1 mm using filler gauge. Experiments were performed on one sample of each type (coated and uncoated). After each test interval, the specimens were rinsed, dried and weighed by an analytical balance with a sensitivity of 0.1 mg to determine mass loss. To plot the erosion curve an average of 5 readings taken for the tested specimen after each interval were used. The topographical characterisation of the post-test coatings was conducted using an Alicona infinite focus microscope (IFM) G4 with 20 x objective at 75 nm vertical resolution.

For comparison of coatings performances, CE experiments were also carried out on commercially deposited monolithic TiN coatings deposited on Ti6Al4V substrates.

3.0 Results and discussions:

3.1 Coating mechanical properties.

The adhesion strength of CrAlYN/CrN deposited on HSS and Ti6AlV substrate was measured by Rockwell C indentation and scratch tests and the results are presented in Figure 1 (a-d). For both coatings, deposited with high and low ion bombarding energies (C1 and C2 coating respectively), optical microscopic observation showed no cracks, delamination or spallation of the coatings around the Rockwell indents confirming superior adhesion between

the coating and the substrate. This superior adhesion strength of the coatings can be rated as grade Class 0 (ISO 26443) equivalent to HF1 (DB test). This is especially important considering the Ti6Al4V substrate (hardness of $HK_{0.25\ N}$ = 405 and Young's Modulus (E) = 152.3± 7.2 GPa) is comparatively softer (Figure 1b). Similarly no spallation of the coatings was evident under scratch tests even though the normal load progressively reached 80 N leading to through thickness perforation (Figure 1d). This excellent adhesion behaviour is mainly attributed to the well-defined crystal structure at the coating-substrate interface provided by the HIPIMS metal ion etching, which promotes the localized epitaxial growth of the coating. Both C1 and C2 coatings had a similar thickness of around 4 µm. The hardness of C1 coating was in the range of 3000 $HK_{0.25N}$ whereas the Young's modulus value (E) was calculated to be around 300 GPa. The C2 coating was found to have a hardness value in the range of 2700 $HK_{0.25\ N}$ as well as reduced Young's modulus (E) value of 275 GPa. Both coatings had nearly similar compressive residual stress values in the range of - 4 ± 0.5 GPa. The commercially sourced TiN coatings had a hardness of 2200 $HK_{0.25N}$, and compressive residual stress value of -2 ± 0.5 GPa. The thickness of the TiN coating was 2.7 µm.

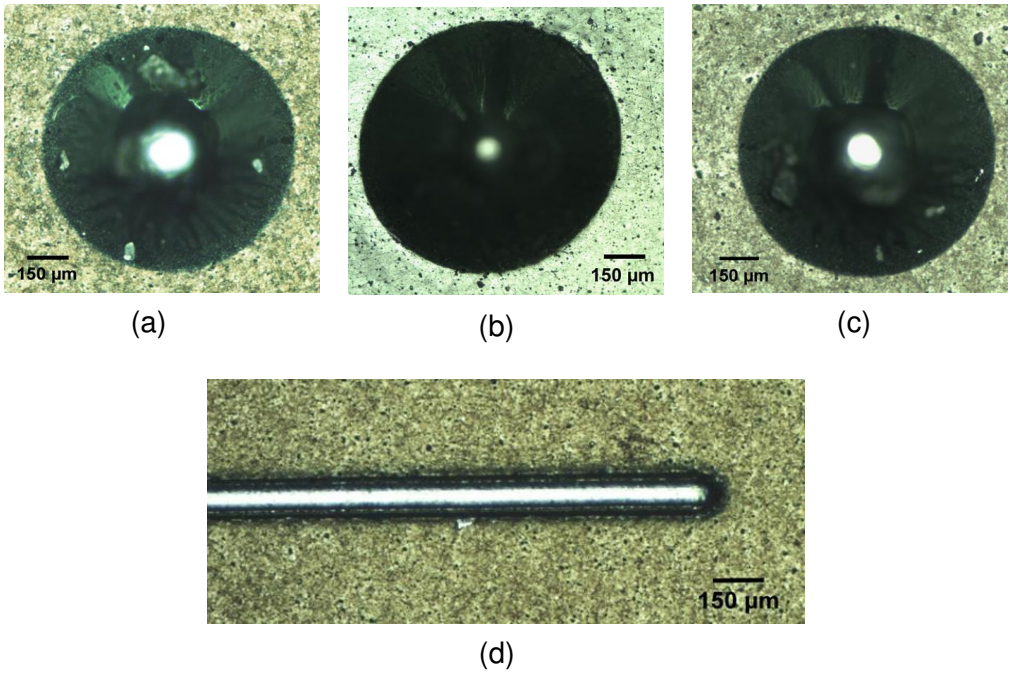

Figure 1 Rockwell C adhesion tests (a) C2 coating on HSS substrate (b) C2 coating on Ti6Al4V substrate, (c) C1 coating on HSS substrate and (d) Scratch test C2 coating on HSS substrate.

3.2 Coating microstructure.

Figure 2a shows the low magnification TEM image of the whole CrAlYN/CrN coating (C2) obtained in a bright field imaging mode. The image shows a surface of the substrate which has been pre-treated (etched) with a metal ion enriched HIPIMS plasma followed by the deposition of a dense CrN base layer (around 250 nm). The interface between the substrate and the base layer was found to be very smooth, sharp and without any defects (neither droplets nor any voids in the interface region), often observed in arc and Argon ion etching respectively, is a typical feature of HIPIMS etching [23]. On top of the base layer, alternating layers of CrAlYN and CrN (bi-layer thickness of approximately 3 nm) have been deposited, Figure 2b, to form the nanoscale multilayer coating. The implantation of metal ions during the etching step leads to the formation of a superior epitaxial coating microstructure that not only is limited to the adjacent base layer but also extends to the top of the coating, [23]. In

this case the epitaxy was evident in Figure 2a wherein wide portions of coating columnar microstructure with a similar colour contrast could be seen extending right from the bottom of the base layer to the top of the coating as the coating synthesised uninterruptedly. The epitaxial microstructure along with smooth, defect free substrate-coating interface leads to superior adhesion bonding. The effect of the high metal ion irradiation during coating synthesis was also visible from the growth of dense and wide columns with flat tops (Figure 2a) as well as the presence of flat and sharp interfaces within the nanoscale multilayers (Figure 2b). This superior dense microstructure along with high adhesion imparts superior barrier and mechanical properties to the coating. The microstructure of the C1 coating also had similar multilayer architecture with anticipated minute changes in the bi-layer thickness, columnar width (figures not included) and texture of the coating due to the different intensity of the ion bombardment during the growth. The monolithic TiN coatings in general had smooth surfaces without any macro-particle defects. FIB cross-sectional studies confirmed the microstructure to be made-up of dome shaped columnar grains, which are typical for sputtered coatings (see Figure 9) but without the nanoscale multilayer stacking as observed in the C1 and C2 coatings.

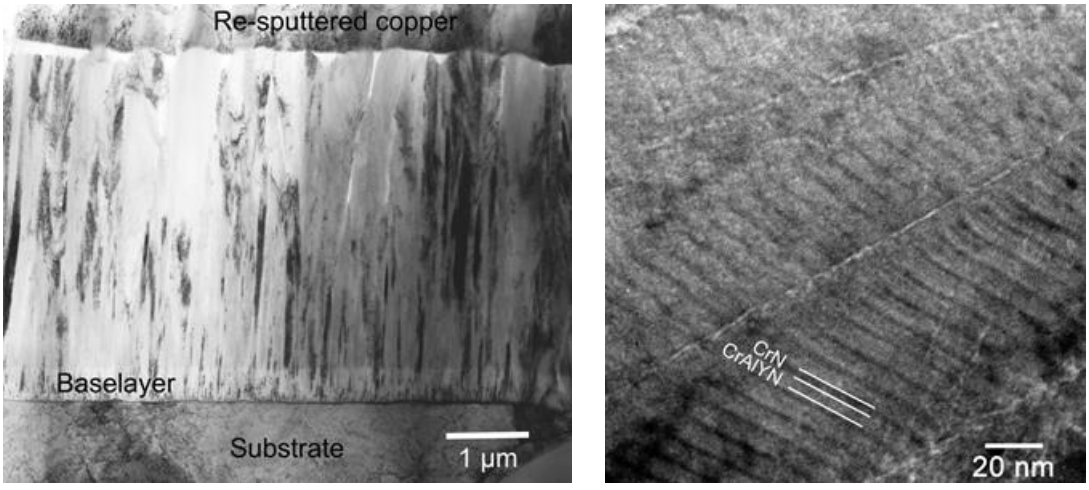

(a) (b)

Figure 2 (a) Bright field TEM image of the whole C2 coating; (b) High magnification bright field TEM image of the multilayer structure consisting of alternating CrAlYN (light contrast) and CrN (dark contrast) nanoscale layers.

3.3 Coating texture.

The texture evolution in CrAlYN/CrN coatings was analysed using X - ray diffraction (θ-2θ, BB geometry) technique. Figure 3 shows BB XRD patterns of the C1 and C2 coatings (SS substrates) deposited with high and low ion bombarding energies. The results indicate that the coatings had a NaCl type f.c.c crystal structure. The CrAlYN/CrN coating deposited with low ion bombarding energy exhibited a strong {111} preferred orientation (as shown in Figure 3 a), in contrast to {200} (as shown in Figure 3 b) for the coating deposited with high ion bombarding energy. It was reported in the literature that the texture in HIPIMS deposited TiN coatings transformed from {111} to {200} while increasing the ion bombardment energy [24]. The increased ion energy influenced the texture of the coatings by enhancing the ad-atom mobility and increasing the flux of atomic nitrogen created by a kinetically-induced dissociation of nitrogen molecules at the substrate surface. The {200} orientation was found to be dominant in the presence of atomic nitrogen and ionized metal flux due to the trapping of Ti on {200} sites through the formation of TiN clusters. It was also reported that {111} orientation was promoted under deposition conditions in which the incident particles are mainly metal atoms and N_2 molecules (non-ionised flux) and Ti is trapped predominantly on {111} sites [24]. Thus compositionally similar C1 and C2 coatings show difference in texture owing to the difference in ion bombardment levels during the coating growth stage.

In turn, the crystalline texture plays a significant role in CE behaviour, grains with (111) orientations resist CE better [8, 25, 26]. The effect of the texture of HIPIMS coating on the CE performance will be further discussed in section 3.5. XRD results on the commercially

sourced monolithic TiN coating also exhibited a f.c.c NaCl structure with a strong {111} texture (Figure 3c).

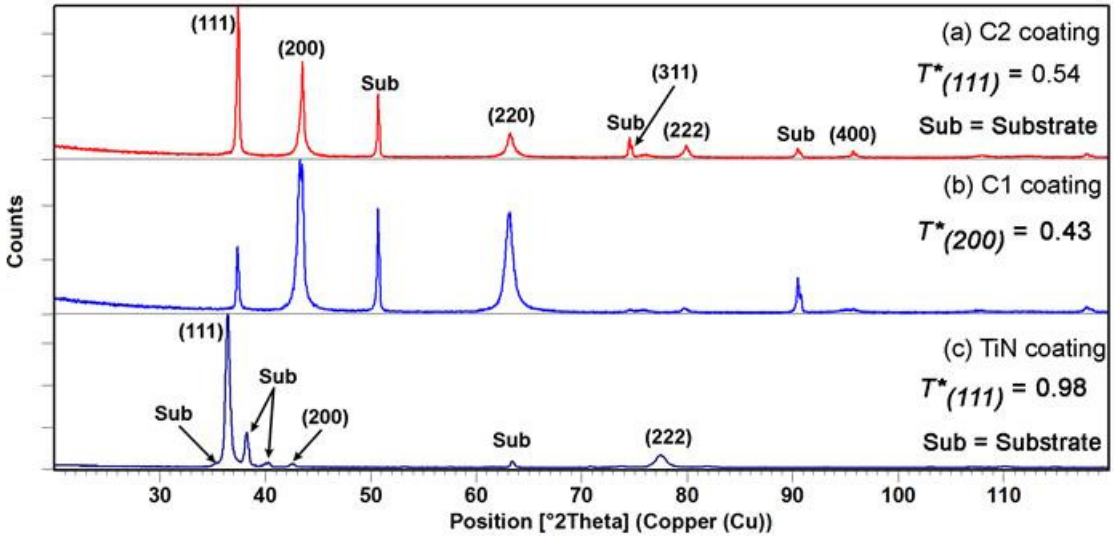

Figure 3 XRD results used for texture analysis of different coatings in this study.

3.4 Cavitation erosion performance of HIPIMS coatings.

Results of the CE tests show that both HIPIMS coated specimens outperform the bare Ti6Al4V substrate, Figure 4. The C2 coating demonstrates significant improvement of CE performance with reduced maximum erosion rate of 0.002 mg/min, comparing to 0.024 mg/min for the substrate material. Furthermore, the incubation period is prolonged more than twice (>240 min) with comparison to that of the substrate Ti6Al4V (120 min), as listed in Table 1. In the case of C1 coating, the incubation period also indicates an improvement of 60 minutes (180 min); however, the erosion rate starts to increase after 150 mins of CE exposure and reaches up to the maximum value of 0.030 mg/min by the end of the test. Both HIPIMS coatings present excellent CE behaviour comparing to the multilayer coatings manufactured by traditional PVD process [27, 28]. This can be attributed to the synergy between

superhardness and a special crack propagation mechanism that enhances the toughness. Additionally, the thin HIPIMS coatings (about 4 microns) outperform thick coatings reported in the literature, such as those deposited by Chemical Vapour Deposition (CVD) [29] and High Velocity Oxy Fuel (HVOF) [30, 31] processes. It is revealed that the thick but porous HVOF coatings demonstrate almost no incubation period under CE. Surface and cross-sectional analysis was conducted to further understand the coating behaviour under CE.

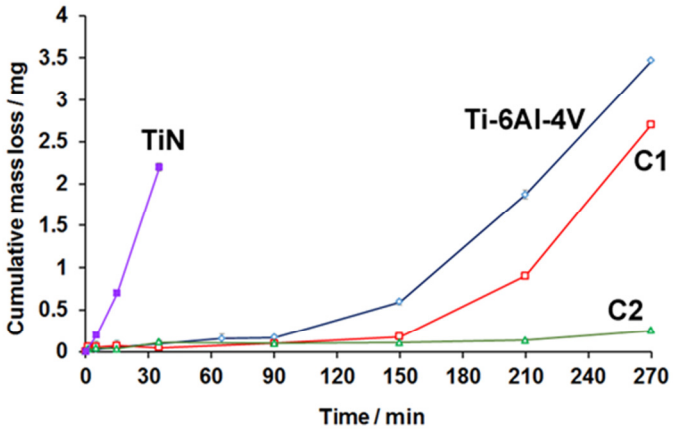

Figure 4 CE results of HIPIMS coatings versus Ti6Al4V substrate and TiN coating.

Coatings	Test facility	Incubation period (min)	Maximum erosion rate (mg/min)	Manufacturing process	Thickness (µm)	Test period (hour)
Ti6AlV4	Vibratory cavitation apparatus	120	0.027	/	/	4.5
C1		180	0.013	HIPIMS	4	
C2		240+	0.002			
CrN/CrCN [27]	Cavitation	30	0.020	PVD	4.3	10

Ti/TiN-4 [28]	tunnel	60	0.004		3.7	
(NiTi/TiCN)0.5 [32]	Vibratory cavitation apparatus	60	0.004		3.32	12
Nanocrystalline diamond [29]		30	0.011	HF-CVD	1	2.5
M6-HV [29]		15.6	0.027	HVOF	134 ± 6	8
WC-CoCr [29]		61.8	0.041		107 ± 12	8
Cr_3C_2-NiCr [31]		0	0.050		30 - 40	8
CoMoCrSi [33]		0	0.125	Plasma spray	/	2
FeNiCrBSiNbW [34]		0	0.150	Arc spray	230	2

Table 1 Comparison of CE performance of HIPIMS coatings with those reported in literatures.

3.5 Cavitation mechanisms.

3.5.1 Incubation period

The CE behaviour of both HIPIMS coatings during incubation period was investigated with FIB/SEM analysis. Figure 5(a-c) show areas of the C1 coating which were subjected to erosion tests conducted for 90 minutes (incubation period) and then subsequently chosen for FIB milling. As observed in Figure 5a, the C1 coating surface was found to be intact without any evidence of intergranular cracking or cohesive fracture or similar coating removal mechanisms. Formation of pits due to localised removal of deposition chamber related

nodular, open void and cone shape coating defects [35] can be seen. On closer inspection at the cross-sectional view, cracks were found at the substrate (as labelled in Figure 5b) and propagating into both the substrate and the coating (Figure 5c). In the case of C2 coating, Figure 5 (d-f), no cracks were found on the surface or on the cross-sections during incubation period.

The coated specimens construct a system with a hard and tough coating applied on a compliant substrate. The hardness of the coatings is nearly up to 8 times higher than those of the substrate. The high impact pressure and stress waves induced by implosion of cavitation bubbles cause deformation in the target material [36–38]. The dislocation density is increased during this process [37]. The nanoscale multilayer structure restrains the mobility of the dislocations; hence, limited plastic deformation occurs. Additionally, the enhanced toughness of the superlattice structured coatings can also contribute to better resistance to cavitation impulse [16, 17]. As the stress waves propagate through the coatings and reach the interface, they would be partially transmitted and partially reflected. The magnitude of the stress waves reaching the interface can vary due to the different coating textures, which will be further discussed in the following section. The transmitted stress waves then interact with the substrate material. The Ti6Al4V substrate demonstrates more compliance with larger grain size (average size 5µm measured by SEM), which can promote the dislocations with more space to move and lead to plastic deformation. The repetition of the process of loading and unloading induced by clouds of microjet impingements leads to a fatigue-like phenomenon, eventually forming cracks in the Ti6Al4V substrate. The fact that we observed subsurface cracks on the C1 coating cross-sections indicates that more stress waves transmitted to the substrate material. While for C2 coating, the crack initiation is delayed. More detailed discussion shown in the following section.

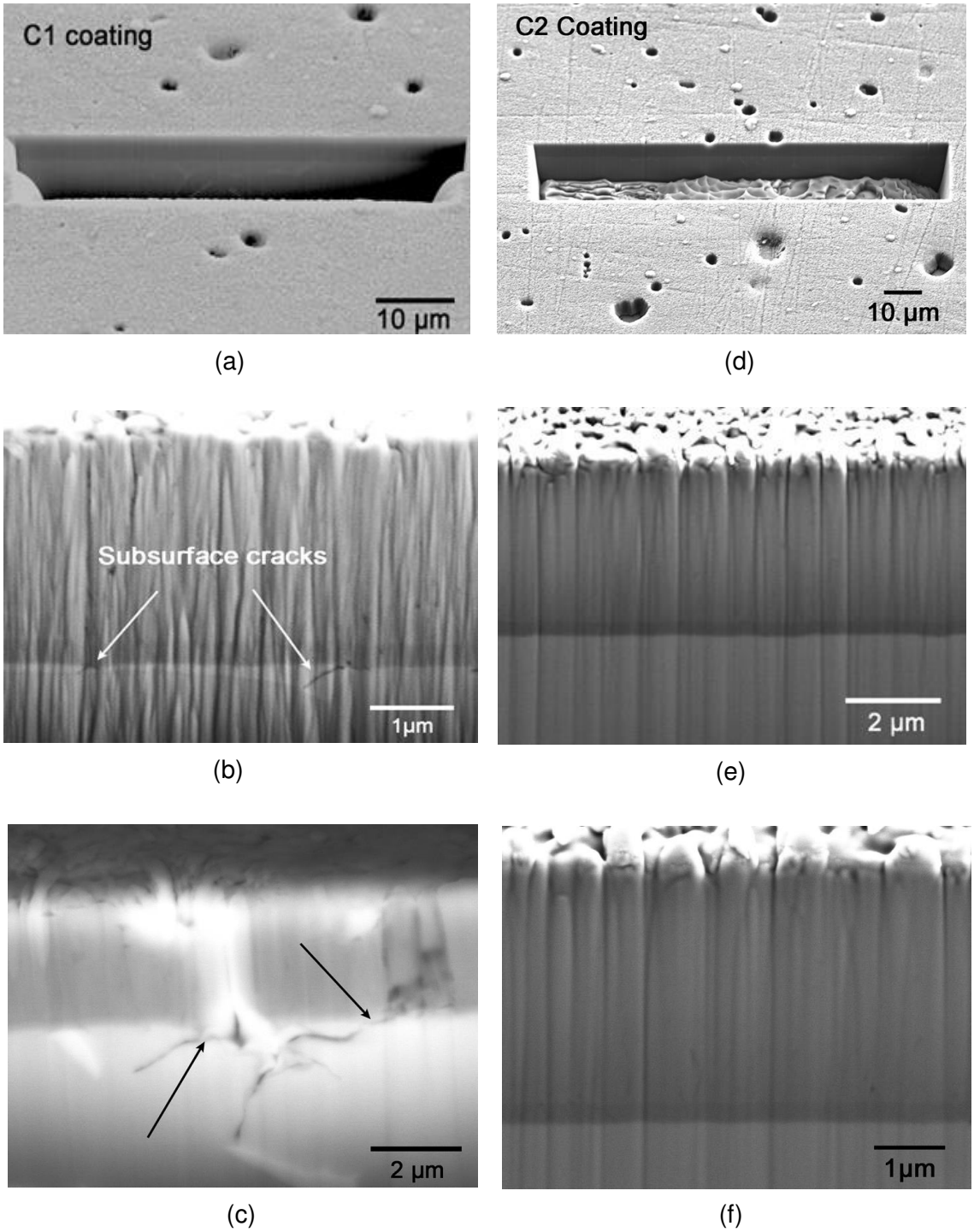

Figure 5 (a), (b) and (c): FIB cross-sections of C1 coating during incubation period; arrows indicate cracks (d), (e) and (f): cross-sections of C2 coating during incubation period.

3.5.2 Advanced stage

The surface profile of the two coatings tested under CE for 270 mins are shown in Figure 6. Material removal was detected at the edge and the centre of the exposed surface of C1 coating (Figure 6a). Whereas for the C2 coating, the surface profile presented in Figure 6b indicates that the damage was localised. These observations were further supported by SEM analysis presented in Figure 7. Coating removal leading to the exposure of substrate surface and its subsequent erosion could be observed in larger quantities in the case of C1 coating (Figure 7a). Whereas in the case of C2 coating (Figure 7b), material removal was much localised and in general very limited damage was observed.

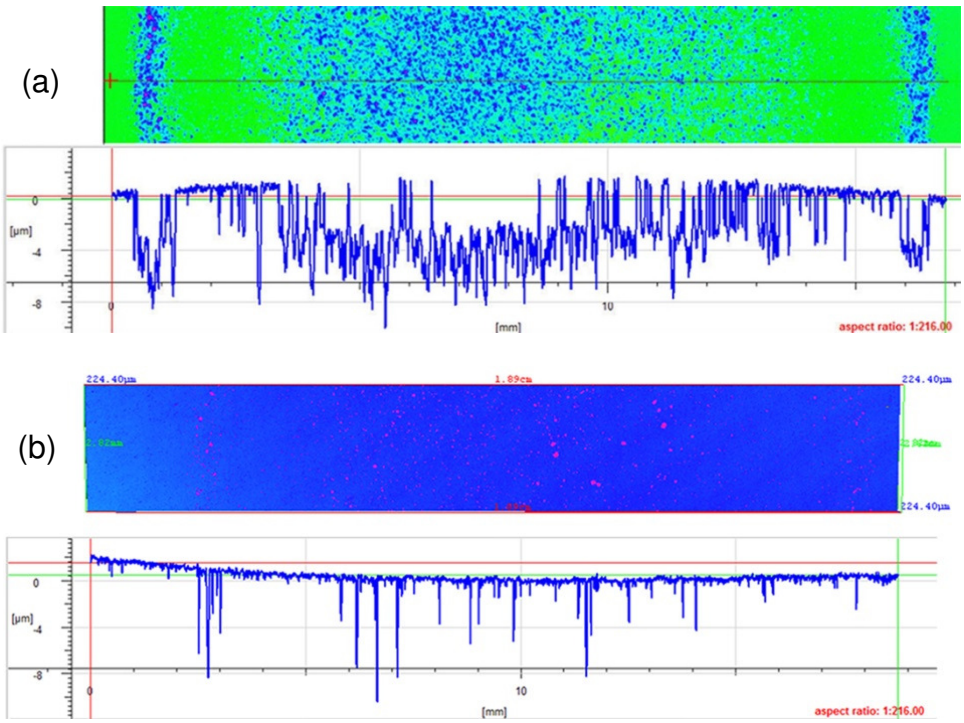

Figure 6 Surface profiles of 270 mins of CE tests: (a) C1 coating; (b) C2 coating.

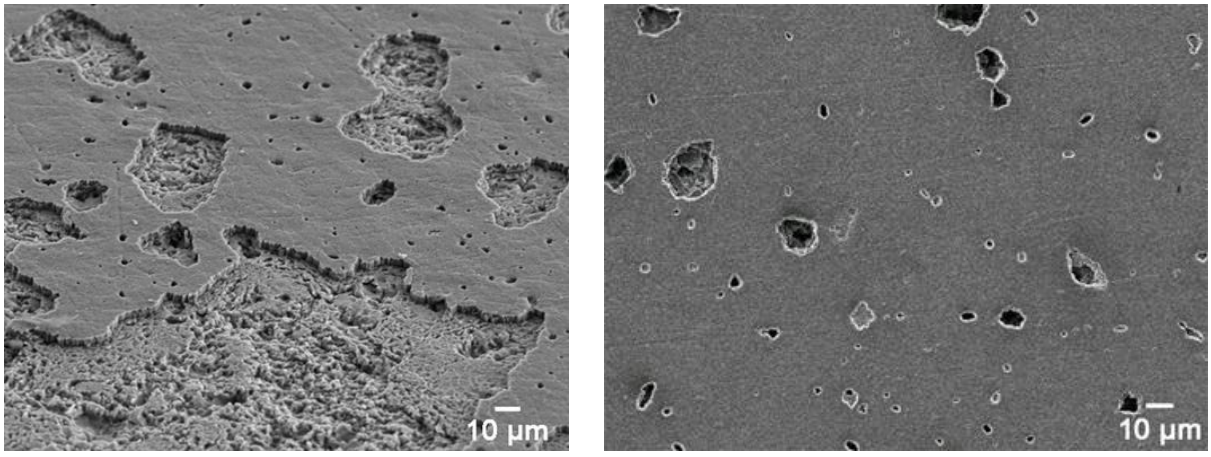

Figure 7 Exposure surface of 270 mins of CE tests: (a) C1 coating; (b) C2 coating.

Cross-sectional investigation through FIB/SEM was conducted to further understand the CE mechanisms of both nanoscale multilayer coatings, as shown in Figure 8. It shows a variation in the level of protection offered by the two coatings in the advanced stages of CE. In the case of C1 coating, lateral growth of the subsurface cracks (near the coating-substrate interface) into the Ti6Al4V substrate was prominently observed, as shown in Figure 8a and 8b. Some of these cracks were also found to traverse into the coating, as labelled in Figure 8a. An erosion crater was formed inside the substrate due to the removal of the substrate material together with the coating, Figure 8c. It can be seen that the coating at the surrounding area was still attached to the substrate surface which clearly indicates that the damage is not adhesion related. In the case of C2 coating, initiation of subsurface cracks (initially absent in the incubation period) was also observed. However, compared to the C1 case the subsurface cracks were much smaller in size and their number density was lower. As expected for a nanoscale multilayer structured coatings crack propagation in a lateral manner was observed due to deflection at the interfaces between the individual nanolayers, see Figure 8d.

It was widely reported that the most common failure mode with coated substrates under CE is through coating delamination, [27, 28, 39]. This is due to the high impact pressure and stress

wave reinforcement induced by repeated implosion of the cavitation bubbles at the coating-substrate interface. The same damage mechanism is also reported in the multilayer coating systems, such as CrN/CrCN [27] and Ti/TiN [28]. It should be noted that the coating-substrate interface of the referenced coatings was not engineered by metal ion implantation. In contrast, both C1 and C2 nanoscale multilayer coatings deposited by HIPIMS demonstrated excellent bonding strength with no coating delamination from the substrate due to the metal ion surface pre-treatment, [20, 23].

It can be further proposed that one of the damage mechanisms in both coatings can be induced by the surface defects formed during the deposition process. These nodular, open void and cone shape coating defects [35] can act as stress raisers for implosion of cavitation bubbles. Then, the continuous actions of shearing and tearing at these sites lead to subsequent material removal, eventually contributing to enhanced local erosion rates. However, this is not considered as the main failure mechanism, since both coatings have similar surface defects but exhibit different CE performance.

It is believed that the formation of cracks in the sub-surface region in the incubation period and the way these cracks propagate, both into the substrate and coating during the advanced stage, seems to be the key to understand the wear mechanism in such system in CE conditions.

As discussed, after a test period of 270 mins, prolonged plastic deformation and crack formation in the substrate of C1 coating was observed, as shown in Figure 8a. This could be attributed to the less effective dissipation of the exerted impact pressure and the stress waves on the {200} oriented crystallographic structure. As the cracks developed in the substrate and coalesce at the subsurface (Figure 8b), material removal can then take place that leads to the formation of erosion craters inside the Ti6Al4V substrate, as seen in Figure 8c. On the other hand, the results indicate that the C2 coating appears to be better equipped to dissipate the

stress waves. This can be correlated to the denser atomic packing of the {111}crystallographic planes, which delay crack initiation in the substrate more effectively as compared to the lower atomic density {200} planes of the C1 coating. This phenomenon has been observed in the past studies on CE applications suggesting that materials with certain crystal orientation demonstrate better resistance to wear and CE [8,25,26]. The experiments further revealed that the efficiency of the elastic energy transport through the material, which depends on its elastic properties, also needs to be considered. In our case, the Young's modulus value (E) of the C1 coating, (E_{C1}= 300 GPa) is greater than that of the C2 coating, (E_{C2}= 275 GPa) therefore we observe more effective elastic energy transport through the C1 coating, resulting in more damage to the underlying substrate material.

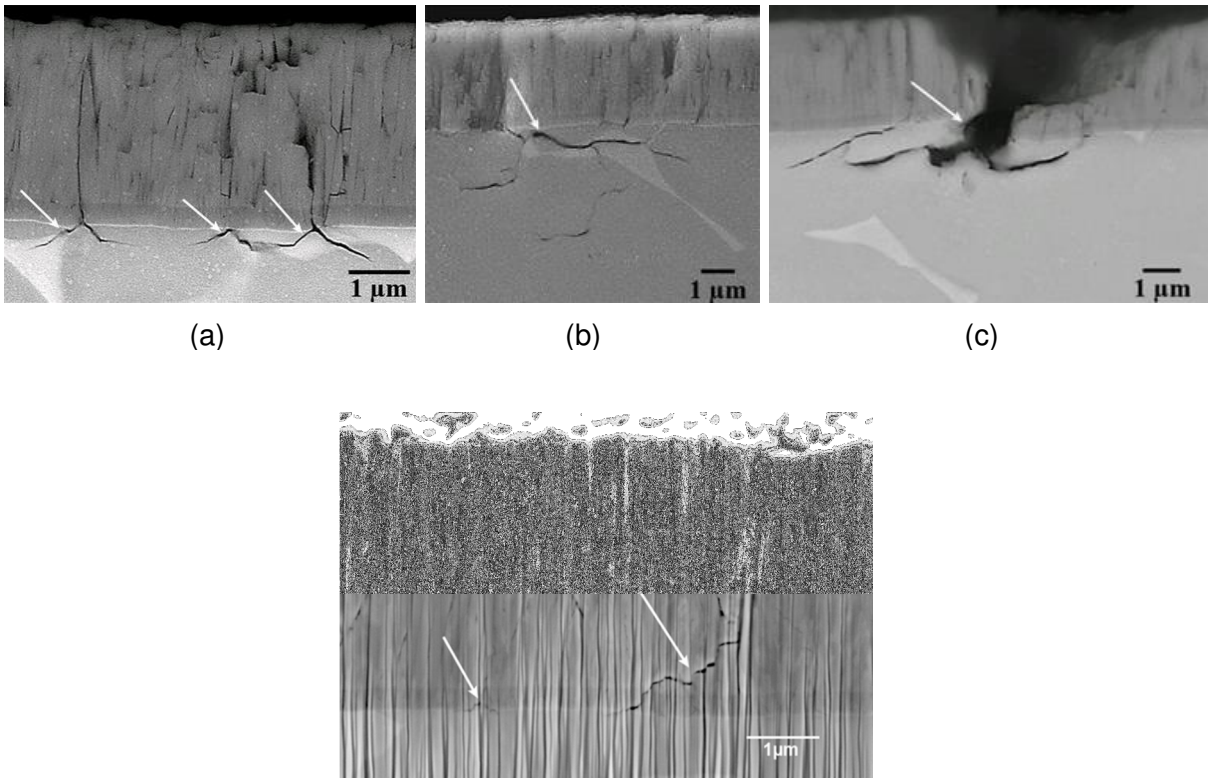

Figure 8 Cross-sectional FIB SEM analysis after 270 mins of CE tests, white arrows indicate the cracks observed in: (a,b,c) C1 coating; (d) C2 coating.

Thus superior coating microstructure, along with the engineered coating texture ({111} dominant) and lower Young's modulus, (E) value seems to define the superior CE resistance of the C2 coating as compared to C1 coating.

3.6 Comparison with monolithic coating.

The beneficial effect of nanoscale multilayer structure can be further demonstrated when comparing the CE performance with a monolithic magnetron sputtered TiN coating on the same Ti6Al4V substrate. The investigated TiN coating exhibits a strong {111} texture. Figure 9(a-b) shows SEM image of the eroded areas of the coating after subjecting it to similar testing conditions as those employed for C1 and C2 coating. The TiN coating failed after 5 mins of CE exposure and the erosion rate exceeded that of the Ti6Al4V substrate after 270 mins of CE tests. As seen in Figure 9a, the TiN coated specimen shows severe damage and loss of coating on large areas of the surface. Formation of inter-columnar cracks as seen in the Figure 9b and eventual coating delamination seems to be the dominant mode of failure. However, unlike the C1 and C2 coating, these cracks appear to originate at the top and propagate vertically along the columnar boundary towards the substrate without any deflection or hindrance. Despite its more favourable {111} texture, owing to the weak bonding between columnar grains, which is an inherited problem of the standard magnetron sputtering deposition renders the coating weak. The results clearly demonstrate that in this case, the monolithically grown TiN PVD coating does not prevent the crack initiation due to the shearing forces encountered in CE as effectively as compared to the nanoscale multilayer structures.

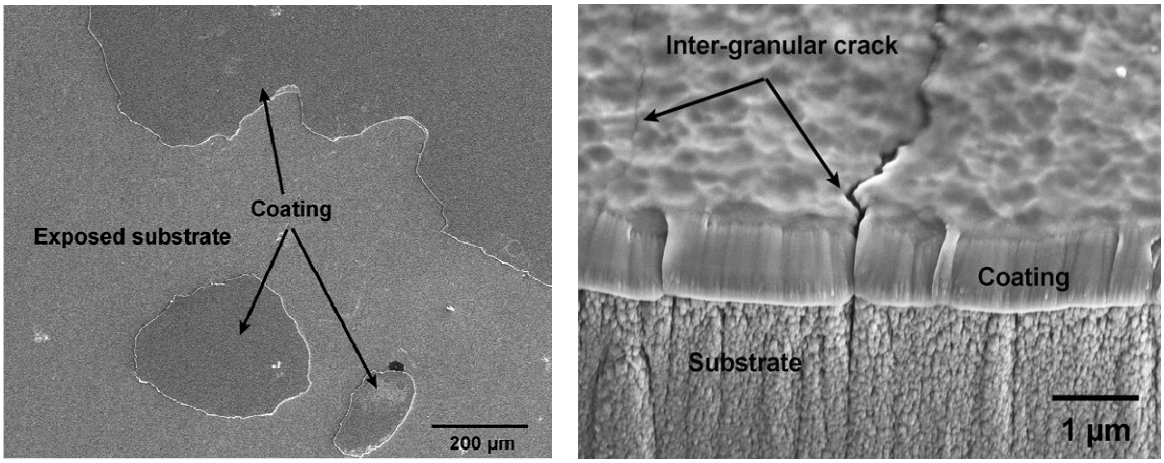

Figure 9 Cavitation erosion studies on TiN coating (a) SEM image of the eroded coating in plan view (b) FIB cross-sectional analysis showing vertical cracking in the coating indicated by white arrows.

4.0 Conclusions:

1. High Power Impulse Magnetron Sputtering (HIPIMS) technology was successfully used to deposit CrAlYN/ CrN coatings utilising nanoscale multilayer structure with high hardness, $HK_{0.25N}$ = 2750, enhanced adhesion (scratch adhesion critical load, L_C= 80 N) and high coating density as shown by FIB/SEM and TEM analyses. In Cavitation Erosion (CE) tests the novel coatings show a factor of 14 lower erosion rates than the base Ti6Al4V substrate and outperformed a range of coatings reported in the literature deposited by PVD, CVD, Plasma spray, HVOF and Arc spray techniques.

2. The research shows that in CE conditions there are significant differences in the coating failure mechanisms between monolithically grown and nanoscale multilayer structured coatings:

- Monolithically grown TiN coatings with {111} texture deposited by standard magnetron sputtering exhibited severe damage after only a few minutes in the CE test where the main failure mechanism was coating delamination due to the weak adhesion bonding and opening of tensile stress inter-columnar cracks due to the sub-dense columnar coating structure.

- The HIPIMS-deposited CrAlYN/CrN nanoscale multilayer structured coatings show no signs of delamination due to the strong metallurgical bonding between the coating and the substrate. Crack initiation was significantly delayed with a 240 minute incubation period achieved in CE tests. FIB/ SEM analyses show clear evidence that the crack propagation mechanism involved crack deflection at the interfaces between the nanolayers, which was highly beneficial for the coating life time.

3. HIPIMS-deposited CrAlYN/CrN coatings with {111} texture grown in conditions of low ion bombardment shows better protection of the substrate material against sub-coating substrate deformation and crack formation as compared to coatings with {200} crystallographic orientation deposited in conditions of higher ion bombardment. It is suggested that the denser atomic packing of the (111) crystallographic planes in the nanoscale multi layered coating better extinguishes the propagation of the elastic shock waves produced in the cavitation attack through the coating material.

4. CE tests revealed that CrAlYN/CrN coatings with lower Young's modulus, (E_{C2} = 275 GPa) provide better protection of the substrate material against crack formation as compared to coatings with higher Young's modulus, (E_{C2} = 300 GPa) due to the less effective elastic energy transport through such materials.

Acknowledgement

This work has been funded by Rolls-Royce plc UK at University of Southampton in collaboration with Sheffield Hallam University.

References

[1] F.J. Heymann, Liquid impingement erosion, ASM Handbook. 18 (1992) 221–231.

[2] ASTM G73-10 (2017), Standard test method for liquid impingement erosion using rotating apparatus, 2017. www.astm.org.

[3] F.J. Heymann, On the time dependence of the rate of erosion due to impingement or cavitation, STP 408 Erosion by Cavitation or Impingement (ASTM International). (1967) 70–110.

[4] F.J. Heymann, High-speed impact between a liquid drop and a solid surface, Journal of Applied Physics. 40 (1969) 5113–5122. doi:10.1063/1.1657361.

[5] J.E. Field, ELSI conference: Invited lecture liquid impact: Theory, experiment, applications, Wear. 233–235 (1999) 1–12. doi:10.1016/S0043-1648(99)00189-1.

[6] S. Hattori, M. Takinami, Comparison of cavitation erosion rate with liquid impingement erosion rate, Wear. 269 (2010) 310–316. doi:10.1016/j.wear.2010.04.020.

[7] T. Keil, P.F. Pelz, J. Kadavelil, J. Necker, W. Moser, D. Christ, Droplet Impact vs . Cavitation Erosion, in: Warwick Innovative Manufacturing Research Centre (WIMRC) 3rd International Cavitation Forum, University of Warwick, UK, 2011: pp. 1–8.

[8] T. Okada, Y. Iwai, Cavitation erosion, JSME International Journal. 33 (1990) 128.

[9] G.F. Schmidtt, Liquid and Solid Particle Erosion, (1979).

[10] M.J. Jackson, J.E. Field, Liquid impact erosion of single-crystal magnesium oxide, Wear. 233–235 (1999) 39–50. doi:10.1016/S0043-1648(99)00193-3.

[11] C.F. Kennedy, R.H. Telling, J.E. Field, Liquid impact and fracture of free-standing

CVD diamond, in: SPIE Conference on Window and Dome TechnologIand Materials VI, 1999: pp. 290–296.

[12] Y.I. Oka, H. Miyata, Erosion behaviour of ceramic bulk and coating materials caused by water droplet impingement, Wear. 267 (2009) 1804–1810. doi:10.1016/j.wear.2009.02.009.

[13] W.F. Adler, Inestigation of Liquid Drop Impacts On Ceramics, 1982.

[14] M. V. Swain, J.T. Hagan, Rayleigh wave interaction with, and the extension of, microcracks, Journal of Materials Science. 15 (1980) 387–404. doi:10.1007/PL00020072.

[15] D. Ma, Liquid impingement erosion performance of deep-rolled Ti-6Al-4V alloy, Concordia University, 2014.

[16] J.W. Hutchinson, Stresses and failure modes in thin films and multilayers, Division of Engineering and Applied Sciences, Harvard University, Cambridge, MA, USA, 1996. doi:10.1.1.366.4011.

[17] R. Hahn, M. Bartosik, R. Soler, C. Kirchlechner, G. Dehm, P.H. Mayrhofer, Superlattice effect for enhanced fracture toughness of hard coatings, Scripta Materialia. 124 (2016) 67–70. doi:10.1016/j.scriptamat.2016.06.030.

[18] A.P. Ehiasarian, Fundamentals and applications of HIPIMS, in: R. Wei (Ed.), Plasma Surface Engineering Research and Its Practical Applications, Research Signpost, Trivandrum, India, 2007: p. 35.

[19] S. Zhang, W. Zhu, TiN coating of tool steels: a review, Journal of Materials Processing Tech. (1993). doi:10.1016/0924-0136(93)90016-Y.

[20] A.P. Ehiasarian, P.Eh. Hovsepian, W.-D.Münz, “A Combined Process Comprising Magnetic Field-Assisted, High-Power, Pulsed Cathode Sputtering and an Unbalanced Magnetron,” EP 1 260 603 A2, DE 10124749, 21.05. 2001, US Pat. 7081186B2, 2005.

[21] D.S. Rickerby, A.M. Jones, B.A. Bellamy, X-ray diffraction studies of physically vapour-deposited coatings, Surface and Coatings Technology. 37 (1989) 111–137. doi:10.1016/0257-8972(89)90124-2.

[22] D.B. Lewis, L.A. Donohue, M. Lembke, W.D. Münz, R. Kuzel, V. Valvoda, C.J. Blomfield, The influence of the yttrium content on the structure and properties of Ti1-x-y-zAlxCryYzN PVD hard coatings, Surface and Coatings Technology. 114 (1999) 187–199. doi:10.1016/S0257-8972(99)00047-X.

[23] A.P. Ehiasarian, J.G. Wen, I. Petrov, Interface microstructure engineering by high power impulse magnetron sputtering for the enhancement of adhesion, Journal of Applied Physics. 101 (2007). doi:10.1063/1.2697052.

[24] A.P. Ehiasarian, A. Vetushka, Y.A. Gonzalvo, G. Sfrn, L. Székely, P.B. Barna, Influence of high power impulse magnetron sputtering plasma ionization on the microstructure of TiN thin films, Journal of Applied Physics. 109 (2011). doi:10.1063/1.3579443.

[25] P. Niederhofer, F. Pöhl, K. Geenen, S. Huth, W. Theisen, Influence of crystallographic orientation on cavitation erosion resistance of high interstitial CrMnCN austenitic stainless steels, Tribiology International. 95 (2016) 66–75. doi:10.1016/j.triboint.2015.11.002.

[26] M. Hajian, a. Abdollah-zadeh, S.S. Rezaei-Nejad, H. Assadi, S.M.M. Hadavi, K. Chung, M. Shokouhimehr, Improvement in cavitation erosion resistance of AISI 316L stainless steel by friction stir processing, Applied Surface Science. 308 (2014) 184–

192. doi:10.1016/j.apsusc.2014.04.132.

[27] A.K. Krella, A. Czyżniewski, A. Gilewicz, A. Krupa, Cavitation erosion of CrN/CrCN multilayer coating, Wear. 386–387 (2017) 80–89. doi:10.1016/j.wear.2017.06.007.

[28] A.K. Krella, Cavitation erosion resistance of Ti/TiN multilayer coatings, Surface and Coatings Technology. 228 (2013) 115–123. doi:10.1016/j.surfcoat.2013.04.016.

[29] G. Bregliozzi, W. Haenni, H. Haefke, Cavitation erosion behavior of nanocrystalline diamond thin films on silicon substrates, Journal of Materials Science. 39 (2004) 6603–6606.

[30] S. Lavigne, F. Pougoum, S. Savoie, L. Martinu, J.E. Klemberg-sapieha, R. Schulz, Cavitation erosion behavior of HVOF CaviTec coatings, Wear. 386–387 (2017) 90–98. doi:10.1016/j.wear.2017.06.003.

[31] G. Taillon, F. Pougoum, S. Lavigne, L. Ton-that, R. Schulz, E. Bousser, S. Savoie, L. Martinu, J. Klemberg-sapieha, Cavitation erosion mechanisms in stainless steels and in composite metal – ceramic HVOF coatings, Wear. 364–365 (2016) 201–210. doi:10.1016/j.wear.2016.07.015.

[32] S. Momeni, W. Tillmann, M. Pohl, Composite cavitation resistant PVD coatings based on NiTi thin films, Materials and Design. 110 (2016) 830–838. doi:10.1016/j.matdes.2016.08.054.

[33] Y. Wang, J. Liu, N. Kang, G. Darut, T. Poirier, J. Stella, H. Liao, M. Planche, Cavitation erosion of plasma-sprayed CoMoCrSi coatings, Tribiology International. 102 (2016) 429–435. doi:10.1016/j.triboint.2016.06.014.

[34] J. Lin, Z. Wang, J. Cheng, M. Kang, X. Fu, Effect of Initial Surface Roughness on Cavitation Erosion Resistance of Arc-Sprayed Fe-Based Amorphous / Nanocrystalline Coatings, Coatings. 7 (2017). doi:10.3390/coatings7110200.

[35] B. Biswas, Y. Purandare, A. Sugumaran, I. Khan, P. Eh, Effect of chamber pressure on defect generation and their in fl uence on corrosion and tribological properties of HIPIMS deposited CrN / NbN coatings, Surface & Coatings Technology. 336 (2018) 84–91. doi:10.1016/j.surfcoat.2017.08.021.

[36] Y. Zhou, F.G. Hammitt, Cavitation erosion incubation period, Wear. 86 (1983) 299–313.

[37] B. Vyas, C.M. Preece, B. Vyas, C.M. Preece, Stress produced in a solid by cavitation, Journal of Applied Physics. 47 (1976). doi:10.1063/1.322584.

[38] T.B. Benjamin, A.T. Ellis, The collapse of cavitation bubbles and the pressures thereby produced against solid boundaries, Philosophical Transactions of the Royal Society A: Mathematical, Physical and Engineering Sciences. 260 (1966) 221–240.

[39] F. Cheng, S. Jiang, Cavitation erosion resistance of diamond-like carbon coating on stainless steel, Applied Surface Science. (2014). doi:10.1016/j.apsusc.2013.11.044.